

Observation of strong phonon-phonon coupling in one-dimensional van der Waals crystals

Shaoqi Sun¹, Qingyun Lin², Yihuan Li¹, Daichi Kozawa³, Huizhen Wu¹, Shigeo Maruyama⁴, Pilkyung Moon⁵, Toshikaze Kariyado^{3*}, Ryo Kitaura^{3*} and Sihan Zhao^{1*}

1. School of Physics, Interdisciplinary Center for Quantum Information, Zhejiang Key Laboratory of Micro-Nano Quantum Chips and Quantum Control, and State Key Laboratory of Silicon and Advanced Semiconductor Materials, Zhejiang University, Hangzhou 310058, China

2. Center of Electron Microscopy, School of Materials Science and Engineering, Zhejiang University, Hangzhou 310027, China

3. Research Center for Materials Nanoarchitectonics (MANA), National Institute for Materials Science (NIMS), 1-1 Namiki, Tsukuba 305-0044, Japan

4. Department of Mechanical Engineering, The University of Tokyo, Tokyo 113-8656, Japan

5. Arts and Sciences, NYU Shanghai, Shanghai 200124, China; NYU-ECNU Institute of Physics at NYU Shanghai, Shanghai 200062, China

Corresponding authors:

KARIYADO.Toshikaze@nims.go.jp

KITAURA.Ryo@nims.go.jp

sihanzhao88@zju.edu.cn

Abstract

The phenomena of pronounced electron-electron and electron-phonon interactions in one-dimensional (1D) systems are ubiquitous, which are well described by frameworks of Luttinger liquid, Peierls instability and concomitant charge density wave. However, the experimental observation of strong phonon-phonon coupling in 1D was not demonstrated. Herein we report the first observation of strong phonon-phonon coupling

in 1D condensed matters by using double-walled carbon nanotubes (DWNTs), representative 1D van der Waals crystals, with combining the spectroscopic and microscopic tools as well as the ab initio density functional theory (DFT) calculations. We observe uncharted phonon modes in one commensurate and three incommensurate DWNT crystals, three of which concurrently exhibit strongly-reconstructed electronic band structures. Our DFT calculations for the experimentally observed commensurate DWNT (7,7) @ (12,12) reveal that this new phonon mode originates from a (nearly) degenerate coupling between two transverse acoustic eigenmodes (ZA modes) of constituent inner and outer nanotubes having trigonal and pentagonal rotational symmetry along the nanotube circumferences. Such coupling strongly hybridizes the two phonon modes in different shells and leads to the formation of a unique lattice motion featuring evenly distributed vibrational amplitudes over inner and outer nanotubes, distinct from any known phonon modes in 1D systems. All four DWNTs that exhibit the pronounced new phonon modes show small chiral angle twists, closely matched diameter ratios of $\frac{3}{5}$ and decreased frequencies of new phonon modes with increasing diameters, all supporting the uncovered coupling mechanism. Our discovery of strong phonon-phonon coupling in DWNTs open new opportunities for engineering phonons and exploring novel phonon-related phenomena in 1D condensed matters.

Phonons are quantized collective lattice motions extended over the entire crystal [1]. They can strongly interact with a rich body of fundamental particles and excitations, giving rise to a wealth of important physical phenomena and consequences [2,3]. Phonon-phonon interactions were first theoretically studied by Peierls in 1929 [4]. They determine fundamental properties of crystals such as the lattice thermal conductivity (κ) as well as the infrared, Raman, and neutron scattering cross sections [1,5,6]. For example, the strong phonon-phonon interactions are directly responsible for the low thermal conductivity in some of the best thermoelectric bulk materials, including PbTe and Bi₂Te₃ containing heavy elements [7-10]. They can also lead to strong reconstruction of phonon spectra, recently demonstrated in reconstructed two-

dimensional (2D) van der Waals moiré structures containing lighter atoms [11-14]. Although strong electron-electron and electron-phonon interactions are ubiquitous in one-dimension (1D), manifesting themselves as behaviors of Luttinger liquid [15,16], Peierls instability [17], Kohn anomaly [18], etc., strong phonon-phonon interactions are so far not observed and realized in 1D condensed matters.

Double-walled carbon nanotubes (DWNTs), comprised of two concentric single-walled carbon nanotubes (SWNTs) that are coupled by van der Waal force, are one of the most ideal platforms to investigate the intriguing coupling effect in 1D. This is because the physical property of component nanotubes is known a priori, provided its structure characterized by the chiral index consisting of two integer vectors, (n_i, m_i) @ (n_o, m_o) of the constituent inner and outer SWNTs, is known. In addition, the combination of inner and outer nanotubes of distinct chirality is only restrained by a largely relaxed inter-tube distance (e.g., 0.32-0.38 nm) and thus can form extremely abundant structural patterns, allowing one to study and engineer the rich coupling effect by examining different DWNT crystals. The extremely large exciton binding energy and divergent density of states (DOS) with van Hove singularities in constituent carbon nanotubes further make optical spectroscopic investigation of inter-tube coupling feasible even at room temperature. Following other works in a perturbative electronic coupling regime [19-21], a non-perturbative coupling was theoretically formulated [22] and recently observed [23] in incommensurate DWNTs. Regarding the phonon coupling, previous experimental studies mostly focused on the radial breathing modes (RBMs) using Raman spectroscopies where blueshifts of RBMs in DWNTs were observed and interpreted as a result of two coupled mechanical oscillators [24-26]. However, all these previous observations [24-26] and theoretical models [24-29] are still limited within the weak-coupling regime: (i) the phonon spectra remain unchanged except for the moderate mode stiffening; (ii) the van der Waals force only weakly hybridizes the intrinsic two RBM modes, making the coupled in-phase and out-of-phase modes predominantly characterized by single wall motion.

Herein we report the first observation of strong phonon-phonon coupling in 1D van der Waals-coupled DWNT crystals. We observe a previously uncharted Raman phonon mode both in one commensurate and three incommensurate DWNT crystals, three out of the four (not entirely sure about the fourth) concurrently exhibiting strongly-reconstructed electronic band structures. Combined with a density functional theory (DFT) calculation on phonon eigenmodes and eigenvalues for a commensurate DWNT (7,7) @ (12, 12), we identify the new phonon mode forms as a result of a nearly degenerate coupling between two transverse acoustic modes (ZA modes) in two constituent nanotubes. The coupling strongly hybridizes the phonon states of inner and outer nanotubes, resulting in evenly distributed vibrational amplitudes over two nanotubes. All DWNTs exhibiting strong phonon-phonon coupling are found to have approximate diameter ratios of $\frac{3}{5}$, small chiral angle twists and that the frequencies of new phonon modes decrease with increasing DWNT diameters.

We combine Rayleigh and resonant Raman spectroscopies to optically probe electronic transitions and phonons in individual DWNTs with known structures that are determined by the electron diffraction technique. The phonon eigenmodes and eigenvalues of nanotubes are calculated using DFT with the van der Waals force included through DFT-D3 method [30-34]. All experimental and calculation details are included in Supplementary Note 1. Most of the structure-identified DWNTs investigated in this study are found in a weak electronic-coupling regime in which the electronic optical transitions show a spectral sum of constituent nanotubes' with a moderate energy shift for each transition, approximately between -200 and + 50 meV [19,20]. Figure 1(a) shows the electron diffraction pattern of a representative DWNT in the weak-coupling regime [35]. Using the procedure developed by Liu et al. [36] and diffraction simulations, we can uniquely determine the structure of this DWNT to be (12, 5) @ (22, 4) (Supplementary Note 2). Its corresponding Rayleigh spectrum is presented in Fig. 1(b) where we observe five distinct optical resonances at about 1.37, 1.44, 1.50, 2.35 and 2.43 eV which can be assigned to M_{11-}^o , M_{11+}^o , S_{22}^i , M_{22-}^o and S_{33}^i with energy shifts of -10, -70, -70, -70 and -170 meV, respectively, where “-” and

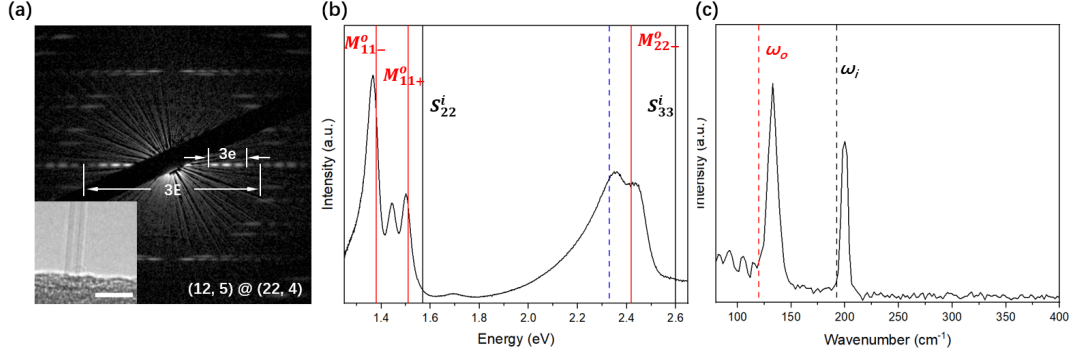


FIG.1. Characterization of a representative weakly-coupled DWNT, (12, 5) @ (22, 4). (a) Electron diffraction pattern, from which the chirality is uniquely determined to be (12, 5) @ (22, 4). The inset is the transmission electron microscopy (TEM) image. Scale bar, 5 nm. (b) Rayleigh scattering spectrum of (12, 5) @ (22, 4). The optical transitions of pristine inner and outer nanotubes are indicated by black and red solid lines, respectively. Excitation energy of ~ 2.33 eV for Raman measurement in (c) is indicated by the blue dashed line. (c) Resonant Raman spectrum of the same DWNT. Two prominent peaks correspond to in-phase (low frequency) and out-of-phase (high frequency) RBM oscillations. The red and black dashed lines indicate the RBM frequencies of pristine outer (ω_o) and inner (ω_i) nanotubes, respectively.

“+” signs stand for the lower and higher branches of metallic nanotubes arising from the trigonal warping effect [37]. Throughout this paper, the optical transitions for semiconducting (metallic) inner and outer constituent SWNTs are denoted as $S(M)_{ii}^i$ and $S(M)_{ii}^o$, respectively, where subscript ii indicates the optical transition originates from the i th paired subbands; the optical transitions for air-suspended inner and outer SWNTs without coupling are indicated by the black and red solid lines, respectively, by referring to a previous literature [38]. Figure 1(c) shows the resonant Raman spectrum of (12, 5) @ (22, 4) in the low frequency range with 532 nm excitation in close vicinity to M_{22}^{o-} transition (blue dashed line in Fig. 1(b)). Two prominent RBM peaks, corresponding to the concerted in-phase (low frequency) and out-of-phase (high frequency) motion of the two walls, are present. We refer to an empirical relation $\omega_{RBM} = \frac{228}{d} (nm\ cm^{-1})$ to obtain RBM peak positions for pristine inner and outer SWNTs that are indicated by the black (ω_i) and red (ω_o) dashed lines throughout this paper where d is the nanotube diameter [39]. The frequencies for the coupled motion are blue-shifted by about 12.9 and 7.7 cm^{-1} when compared with the pristine counterparts, being consistent with previous reports which modeled it as two mechanical oscillators coupled by van der Waals force [24-27].

In this study, we scrutinize 31 individual DWNTs with inner tube diameter ranging from 0.95 to 2.58 nm and with diameter difference from 0.647 to 0.752 nm. Figures 2(a) and 2(b) summarize the RBM shifts (compared to pristine nanotubes) and distribution of chiral angles for 31 DWNTs in this study. In Figs. 2(a) and 2(b) the absolute twist angle (i.e., chiral angle difference between two constituent nanotubes) increases with increasing N . A complete dataset for 31 DWNTs is summarized in Supplementary Table 1. RBM shifts for all DWNTs fall into a range between $+5 \text{ cm}^{-1}$ and $+30 \text{ cm}^{-1}$ (Fig. 2(a)). 10 out of 31 DWNTs ($N = 3, 4, 6, 11, 12, 13, 18, 22, 28, 31$) show only one RBM oscillation which is presumably caused by the off-resonance condition (Supplementary Table 1).

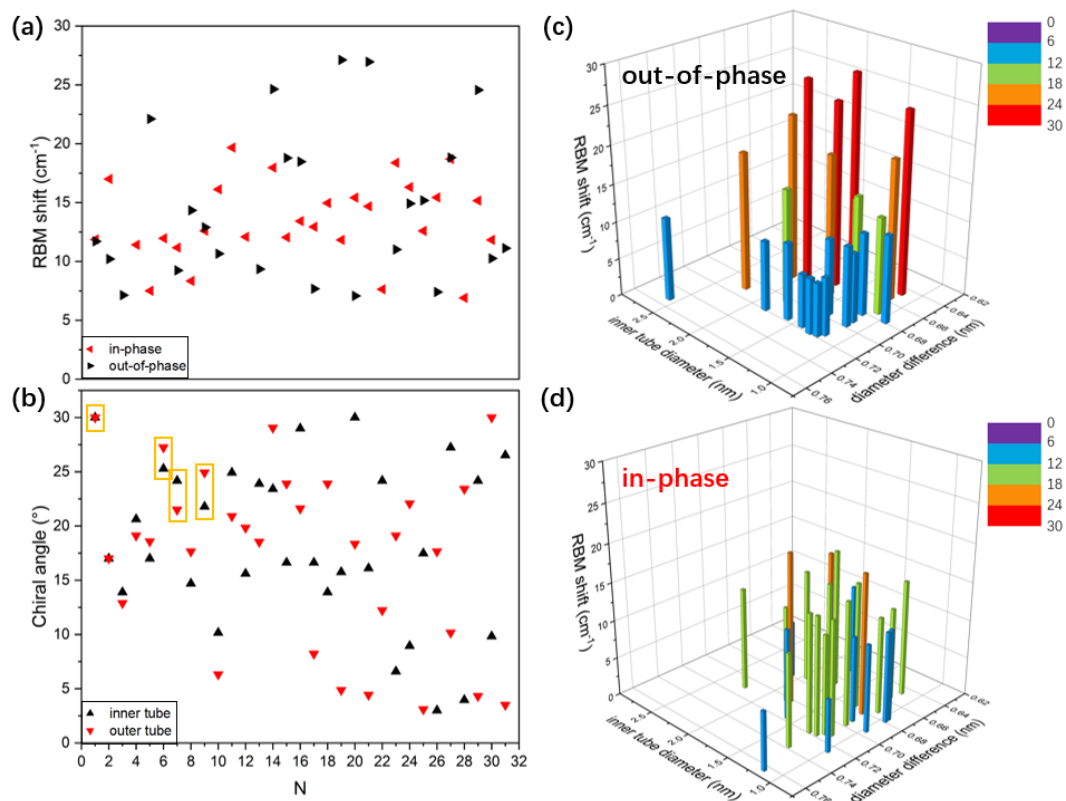


FIG.2. Statistics of RBM oscillations for 31 DWNTs. (a, b) Frequency shifts of RBM oscillations compared with those of pristine SWNTs (a) and chiral angle distribution (b) for 31 individual DWNTs with increasing twist angles from $N = 1$ (0°) to $N = 31$ (23.02°). (c, d) Frequency shifts of out-of-phase (c) and in-phase (d) RBM oscillations as a function of inner tube diameter and diameter difference between inner and outer tubes.

We replot the same RBM shifts (Figs. 2(a)) of out-of-phase (Fig. 2(c)) and in-phase (Fig. 2(d)) RBM oscillations as a function of both inner tube diameter as well as

diameter difference between inner and outer nanotubes. A clear tendency is observed for the out-of-phase oscillations in Fig. 2(c): the frequency shift increases with increasing (inner) tube diameter and with decreasing inter-tube distance. A much weaker effect is present for the in-phase oscillations in Fig. 2(d), which is presumably due to the more significant influence of environment effect on outer nanotube that dominates the in-phase motion. More detailed discussion on the trend shown in Figs. 2(c) and 2(d) are shown in Supplementary Note 3.

The most striking finding of this work is the observation of nascent and uncharted phonon modes that arise from truly 1D strong phonon-phonon coupling effect (Fig. 3). Such new phonons are observed in one commensurate DWNT ($N = 1$) and three incommensurate DWNTs ($N = 6, 7, 9$), all having small twist angles as marked in Fig. 2(b) by the gold frames. In addition to this main finding, we also observe the drastic electronic band structure change of a commensurate DWNT for the first time (Fig. 3(b)), which is notoriously difficult and has long been sought for a few decades. The strong electronic coupling for commensurate and incommensurate DWNTs will be addressed in a separate work.

We identify a commensurate DWNT with chirality of $(7, 7) @ (12, 12)$ ($N = 1$) whose electron diffraction and TEM image are presented in Fig. 3(a) (simulated result shown in Supplementary Fig. 1). As seen from its Rayleigh spectrum in Fig. 3(b), two peaks at about 1.55 and 2.45 eV can be associated with the two optical resonances of M_{11}^o and M_{11}^i for pristine (12,12) and (7,7) SWNTs, respectively. The strong inter-tube electronic coupling is signified by the pronounced peak at ~ 2.05 eV (indicated by the gold frame). This peak (or peaks) is not attributable to any optical transition(s) from the pristine constituent SWNTs. It comes from the strong electronic coupling induced by the commensurate atomic registry. Figure 3(c) shows the resonant Raman spectrum of $(7,7) @ (12,12)$ at low frequency region excited at 514 nm (blue dashed line in Fig. 3(b)). We observe three pronounced Raman peaks at ~ 126.7 , ~ 151.9 and ~ 252.0 cm^{-1} , rather than two as seen in Fig. 1(c). Two peaks at high frequency are the in-phase and out-of-phase RBM oscillations and exhibit frequency blue shifts of ~ 11.8 and ~ 11.8

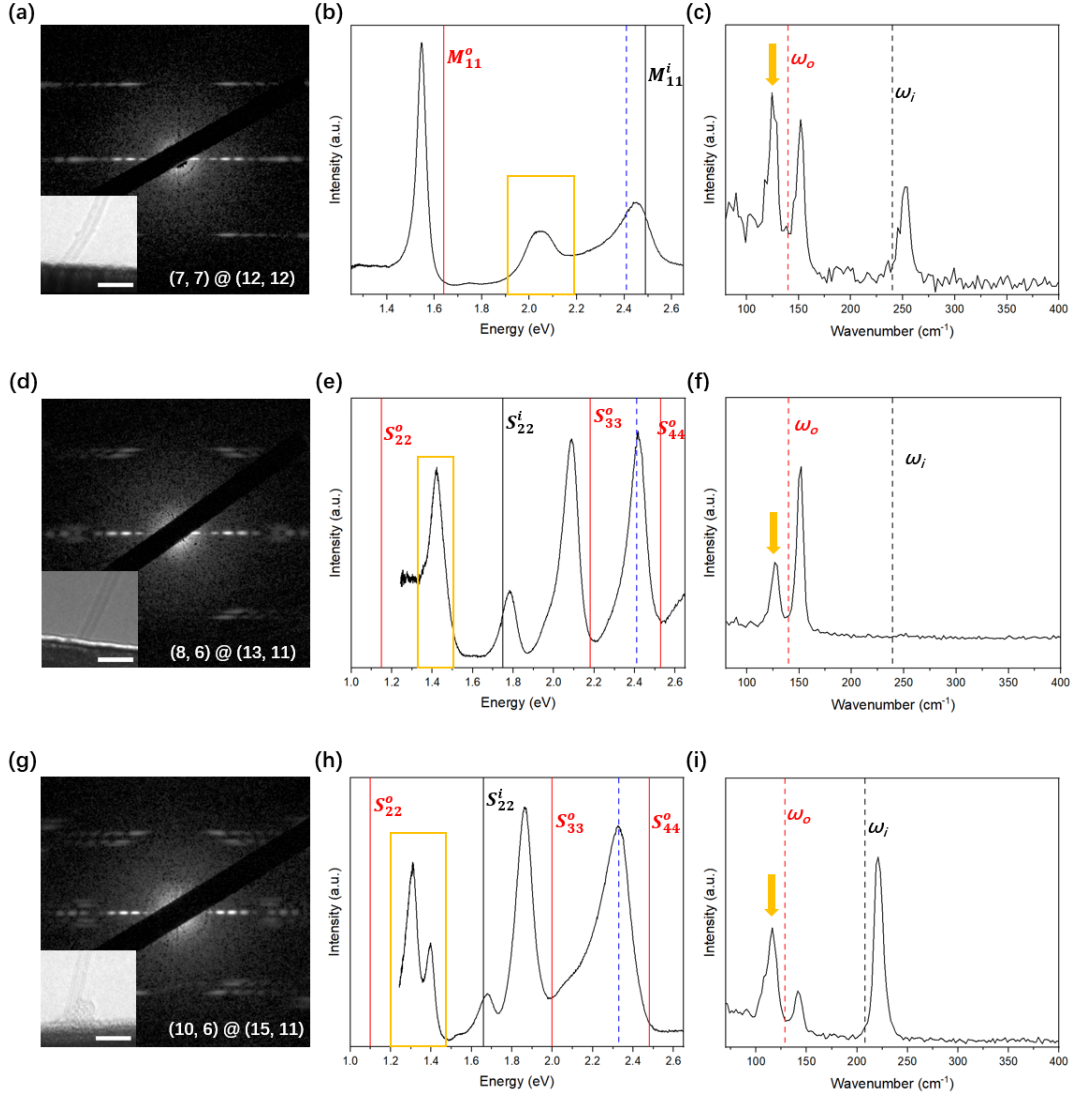


FIG.3. Emergent phonons in strongly-coupled commensurate and incommensurate electron lattices. (a, b, c) Electron diffraction pattern, Rayleigh and resonant Raman spectra of DWNT (7, 7) @ (12, 12). (d, e, f) Electron diffraction pattern, Rayleigh and resonant Raman spectra of DWNT (8, 6) @ (13, 11). (g, h, i) Electron diffraction pattern, Rayleigh and resonant Raman spectra of DWNT (10, 6) @ (15, 11). The inset of each electron diffraction pattern is the corresponding TEM image. Scale bar, 5nm. In Rayleigh spectra, the electronic transitions of pristine inner and outer nanotubes are indicated by the black and red solid lines, respectively. In resonant Raman spectra, the RBM frequencies of pristine inner and outer nanotubes are indicated by the black and red dashed lines, respectively, where the excitation energies are indicated by the blue dashed lines in the corresponding Rayleigh spectra. The gold frames and arrows in Fig. 3 indicate the electronic transitions and new phonon modes arising from strong inter-tube coupling.

cm^{-1} when compared with the RBMs for two pristine inner and outer nanotubes (indicated by the black and red dashed lines). However, the presence of a strong Raman peak at $\sim 126.7 \text{ cm}^{-1}$, which is indicated by the gold arrow, is totally surprising. It cannot

be explained by the coupled oscillator model since it would only yield two blue-shifted phonon modes. We also use a different laser energy to excite the same commensurate DWNT, and we find that this new phonon mode is persistent without showing frequency shift (Supplementary Fig. 2). The Raman spectrum of (7,7) @ (12,12) at high frequency region including the G mode is shown in Supplementary Fig. 3.

Figures 3(d), 3(e) and 3(f) show the electron diffraction, Rayleigh spectrum and resonant Raman spectrum for an incommensurate DWNT with chirality of (8,6) @ (13,11) ($N = 6$). The Rayleigh spectrum in Fig. 3(e) shows that although the three optical transitions at high energy side can be attributed to S_{22}^i , S_{33}^o and S_{44}^o with energy shifts of about +30, -90 and -110 meV, the low energy peak marked by the gold frame yields a significantly larger energy blueshift of about +270 meV when compared with the pristine S_{22}^o (red line). This observation signifies a nontrivial electronic coupling in (8,6) @ (13,11). In fact, this incommensurate DWNT belongs to the “strong-coupling” case where the moiré potential can substantially mix states between two nanotubes [22] (Supplementary Note 4). Very interestingly, in Fig. 3(f) we also observe a new Raman peak (marked by the gold arrow) in this incommensurate DWNT. We emphasize that this new phonon mode has the exactly same energy as for the commensurate (7,7) @ (12,12) (Fig. 3(c)). Given that two DWNTs have almost identical diameters, inter-tube distances as well as small twists (Table 1&S1), this observation hints at the same physics at work for the new phonon modes emerging in Figs. 3(c) and 3(f). The coupled in-phase oscillation shows a frequency blueshift of $\sim 12.0 \text{ cm}^{-1}$ with respect to the pristine RBM of (13,11) (red dashed line in Fig. 3(f)), whereas the out-of-phase counterpart is not observed presumably because the excitation is not in resonance with that of the constituent inner (8,6) (blue dashed line in Fig. 3(e)). We show Raman G mode of (8,6) @ (13,11) in Supplementary Fig. 4.

We observe a similar new phonon mode in a slightly larger incommensurate DWNT with chirality of (10,6) @ (15,11) ($N = 9$) as shown in Fig. 3(i) in addition to the in-phase and out-of-phase oscillations. The new phonon mode that is indicated by the gold arrow in Fig. 3(i) is observed at $\sim 116.1 \text{ cm}^{-1}$ using 532 nm excitation. This phonon

energy is slightly lower than those seen in Figs. 3(c) and 3(f). The new phonon mode retains with a different laser excitation (Supplementary Fig. 5). The corresponding G mode data is shown in Supplementary Fig. 6. The electron diffraction and Rayleigh spectrum of (10,6) @ (15,11) are represented in Figs. 3(g) and 3(h), respectively. Figure 3(h) also demonstrates the “strong-coupling” of the electronic states in (10,6) @ (15,11) as highlighted by the gold frame (see details in Supplementary Note 5).

Supplementary Figure 7 presents a fourth DWNT ($N = 7$) with chirality of (10,7) @ (17,10) that also shows a similar new phonon mode. This DWNT has an even larger diameter and the new phonon mode appears at an even lower frequency of $\sim 97.5 \text{ cm}^{-1}$ (Table 1&S1). In Supplementary Fig. 8 we further find that the new phonon mode in (10,7) @ (17,10) shows a favorable polarization on the ZZ configuration and vanishes in the ZX configuration where ZZ means the incident and outgoing fields are polarized along tube axis and ZX means the incident and outgoing fields are polarized along the tube axis and along the tube circumference. This indicates that the observed new phonon mode is not E_{1g} symmetrywise, but likely to be A_{1g} symmetrywise as the same for the pristine RBMs [29].

In order to pinpoint the origin of the observed new phonon modes in DWNT crystals, we carry out DFT calculations to obtain the phonon eigenmodes and eigenvalues at frequency region of interest. The DFT calculations are performed on the commensurate (7, 7) @ (12, 12) case because of the high computation cost for incommensurate DWNTs with small twists. Our calculations start from a fully relaxed lattice structure of (7, 7) @ (12, 12) in which van der Waals force is captured by the DFT-D3 type correction. The calculated phonon eigenmodes and eigenvalues between 95 cm^{-1} and 255 cm^{-1} are listed in Fig. 4(d). The coupled vibrational eigenmodes and eigenvalues are shown in the middle row, whereas those for the pristine inner and outer nanotubes are shown in the top and bottom rows. Figure 4(c) highlights some of the phonon eigenmodes shown in Fig. 4(d) that are directly relevant to the experiment (Fig. 3(c)). Our DFT calculations in Fig. 4(d) quantitatively match the experimental results in Fig. 3(c) for two pristine RBMs of (7,7) (~ 239.5 vs 240.3 cm^{-1}) and (12,12) (~ 142.5

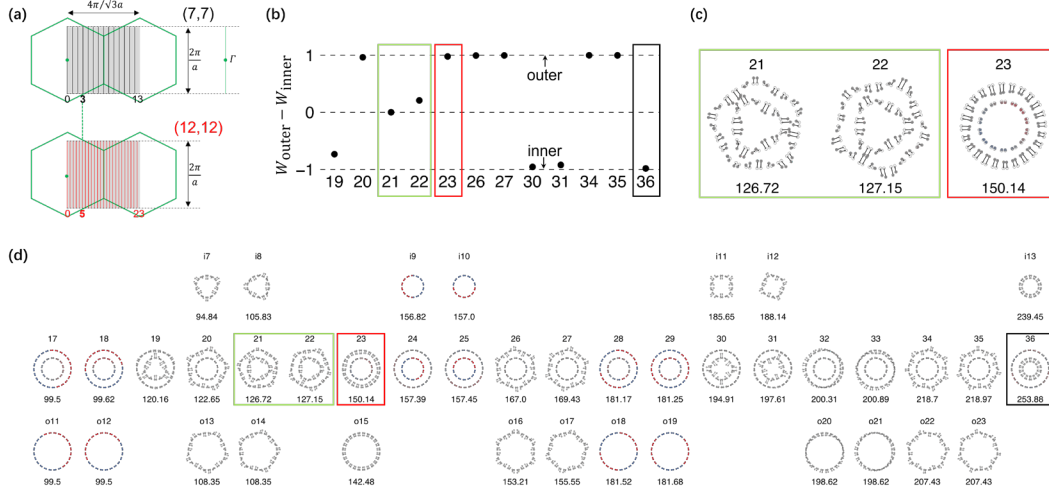


FIG.4. DFT calculations on the phonon eigenmodes and eigenvalues for the van der Waals-coupled commensurate (7,7) @ (12,12). (a) Zone folding (ZF) representation for the first Brillouin zone of (7,7) and (12,12). The green dashed line highlights $l = 3$ of inner nanotube coincides with $l = 5$ of outer nanotube, leading to a nearly-degenerate strong phonon coupling in energy and momentum. The length of graphene unit cell is denoted by a . (b) Calculated weight distribution (W) of eigenmodes for the coupled and uncoupled (7,7) @ (12,12) (see details in the main text). $W \sim -1$ and $W \sim 1$ means the pure motion of inner wall and outer wall. $W \sim 0$ is found for modes 21 and 22 (marked by the green frame), indicative of a strongly hybridized character. (c) Zoomed view of eigenmodes that are marked by the green and red frames in (d). (d) Calculated phonon eigenmodes and eigenvalues between 95 cm^{-1} and 255 cm^{-1} . The coupled eigenmodes are shown in the middle row, while those for pristine inner and outer nanotubes are shown in the top and bottom rows. The new phonon mode observed in experiment (Fig. 3(c)) is marked by the green frame.

vs $\sim 140.05 \text{ cm}^{-1}$) as well as for the coupled in-phase (~ 150.1 vs $\sim 151.9 \text{ cm}^{-1}$) and out-of-phase (~ 253.9 vs $\sim 252.0 \text{ cm}^{-1}$) oscillations in DWNT (7,7) @ (12,12). Given that our Raman measurement uncertainty is about $1\text{--}2 \text{ cm}^{-1}$, the agreement between our experiment and DFT calculation is remarkable. The calculated in-phase (23 in red frame) and out-of-phase (36 in black frame) eigenmodes also verify their weakly-coupled characters. All these results confirm the high fidelity and accuracy for both experiment and theory.

Translational and rotational boundary conditions allow a phonon of an isolated SWNT to be specified by three quantum numbers (q, l, j) . Here q is the wave number associated with the translational periodicity along the tube axis, l is the angular quantum number associated with the rotational periodicity along the circumferential direction and it takes on N integer values $l = 0, 1, 2, \dots, N - 1$ with N being the number of

N	chirality	inner d (nm)	outer d (nm)	inter-tube distance (nm)	twist angle (°)	diameter ratio	$l \times \frac{2}{d}$ in/out (nm ⁻¹)	new mode (cm ⁻¹)
1	(7, 7) @ (12, 12)	0.949	1.628	0.340	0	0.583	6.322/6.143	126.7
4	(8, 6) @ (13, 11)	0.953	1.629	0.338	1.96	0.585	6.296/6.139	126.7
5	(10, 6) @ (15, 11)	1.096	1.770	0.337	3.13	0.619	5.474/5.650	116.1
6	(10, 7) @ (17, 10)	1.159	1.851	0.346	2.69	0.626	5.177/5.402	97.5

Table 1. Summary of four DWNTs showing new phonon modes in this work.

hexagons in the SWNT unit cell, j is one of the six phonon branches for a given (q, l) in 2D graphene Brillouin zone [40]. This is known as the zone folding (ZF) scheme [41], and its representation for pristine (7,7) and (12,12) nanotubes within the nanotube first Brillouin zone is schematically shown in Fig. 4(a). We note that all the phonon eigenmodes in Fig. 4(d) are Γ point phonons of the folded 1D subbands and that the RBM modes for pristine SWNTs cannot be obtained with the ZF scheme [42].

Our DFT calculations in Fig. 4(d) reveal that two phonons at ~ 126.7 (21) and ~ 127.2 cm⁻¹ (22) (also see in Fig. 4(c)) closely match the experimentally observed one at ~ 126.7 cm⁻¹ (gold arrow in Fig. 3(c)). It shows that modes 21 and 22 result primarily from a mode coupling between $i8$ and $o13/o14$ that vibrate at very close frequencies ($i7$ makes a small contribution). A careful mode examination shows that $i7$ and $i8$ for (7,7) constitute approximately three periods along the tube circumference, whereas $o13$ and $o14$ for (12,12) consist of five periods. They are 1D quantization of the transverse acoustic modes (ZA modes) of 2D graphene with $l = 3$ for inner and $l = 5$ for outer nanotubes, respectively (Fig. 4(a)). Notably, the diameter (d) ratio between (7,7) and (12,12) is $0.949/1.628=0.583$ (Table 1&S1), a value that is very close to $\frac{3}{5}$. This immediately means that the physical quantity $l \times \frac{2}{d}$, that is, the vertical distance from Γ point to the l th cutting line, is nearly the same between inner and outer SWNTs (Fig. 4(a)). This also means that the two phonon states should be nearly degenerate in energy within the ZF scheme which is also demonstrated in Fig. 4(d). Supplementary Figure 9 further plots the calculated ZA mode eigenvalues as a function of l for (7,7) and (12,12) where we observe that the eigenvalues increase with increasing l and that $l = 3$ for (7,7) and $l = 5$ for (12,12) form a nearly degenerate pair in energy. Table 1 summarizes the

four DWNTs showing new phonon modes in this work: (i) diameter ratio close to $\frac{3}{5}$ is observed for all the four DWNTs; (ii) the $l \times \frac{2}{d}$ values are very close between inner and outer nanotubes in each DWNT and they decrease with increasing DWNT diameters; (iii) the observed new phonon modes decrease in frequency with increasing DWNT diameters and with increasing averaged $l \times \frac{2}{d}$ values; (iv) all the four DWNTs have relatively small twists, guaranteeing parallel cutting lines of phonon states between their own inner and outer nanotubes. All these jointly experimental and theoretical evidences suggest a strong phonon-phonon coupling picture: a phonon state of inner SWNT at $(0, 3, j)$ strongly hybridizes with another phonon state of outer SWNT at $(0, 5, j)$.

This coupling is very strong because the two interacting phonon states are nearly degenerate in both energy (Supplementary Fig. 9) and momentum (Table 1). As a measure of the coupling strength, we plot phonon eigenmode weight distribution W for selected modes in Fig. 4(b). Writing the displacement of i th atom (relative to its equilibrium position) as \vec{u}_i , we define $W = W_{\text{outer}} - W_{\text{inner}}$, with $W_{\text{outer}} = \sum_{i \in \text{outer}} |\vec{u}_i|^2$ and $W_{\text{inner}} = \sum_{i \in \text{inner}} |\vec{u}_i|^2$. In practice, a phonon eigenvector is normalized as $\sum_i |\vec{u}_i|^2 = 1$, and then $W \sim 0$ indicates strong mixing between inner and outer nanotube, whereas $W \sim +1$ corresponds to pure outer mode and that $W \sim -1$ corresponds to pure inner mode. Compared with the other modes, the new phonon modes (21 and 22) show significantly smaller $W \sim 0$ and evenly distributed vibrational amplitudes over inner and outer SWNTs are observed (Fig. 4(c)), indicative of highly hybridized nature. By contrast, the conventional in-phase (23) and out-of-phase oscillations (36) show $W \sim +1$ and $W \sim -1$, characteristic of motion predominantly from single wall.

The phonon mode shapes (21 and 22 in Figs. 4(c) and 4(d)) infer that the strongly hybridized modes are Raman active symmetrywise. Firstly, we notice that the in-phase RBM (23) gets distorted in a 5-fold (pentagonal) rotational symmetric way, which indicates the symmetry of DWNT allows mixing between pure RBM (inner nanotube,

in this case) and pentagonal modes. (The pentagonal distortion was found in a previous work without explanation [27]. A possible explanation for the pentagonal distortion is described in Supplementary Note 6.) On the other hand, we have seen that the strongly hybridized modes show pentagonal shapes, which infers that these modes can also be Raman active. Note that 7 and 12 have no common divisor, and therefore, there is no rotational symmetry (even discrete ones) along the axis of (7,7) @ (12,12) in a strict sense. This allows modes with different angular momenta to couple in principles, but the coupling effect is prominent only when l satisfies a matching condition as explained above. Inversely speaking, if nanotubes are modeled as continuum elastic tubes, pure RBMs cannot mix with pentagonal modes, since they are distinguished by the continuum rotational symmetry. This could suggest importance of microscopic electronic structures and a complex interplay between the phononic and electronic structures, in accordance with our observation that new Raman mode is attendant with strong coupling features in Rayleigh spectrum.

All DWNTs satisfying the electronic “strong-coupling” condition show signs of the strong phonon-phonon coupling in this work, albeit the connection between the two is not fully understood yet. Although all the new phonon modes reported in this work are founded to have a diameter ratio close to $\frac{3}{5}$, the rich body of DWNT crystals may allow an abundance of strong phonon-phonon coupling with diameter ratios other than $\frac{3}{5}$. We theoretically investigate the phonon eigenmodes and eigenvalues of another hypothesized yet realistic commensurate DWNT (5,5) @ (10,10) with a diameter ratio of $\frac{1}{2}$ (Supplementary Fig. 10). The strong phonon-phonon coupling is not present in this case because of the large energy mismatch. This hints that the curvature effect plays a role beyond the quantum confinement we have considered so far (also see Supplementary Fig. 9). The synergistic quantum confinement and curvature effects were proposed to make the atomic displacements aligned along the tube axis (LO phonons) and tube circumference (TO phonons) in chiral nanotubes [40]. This intriguing preference may facilitate the strong phonon coupling effect in

incommensurate DWNTs with small twists. Understanding the precise role of moiré effect and determining the nanotube handedness will also complement the in-depth understanding of this topic.

In conclusion, we report the discovery of strong phonon-phonon coupling effect in 1D condensed matter systems. We observe new phonon modes of strongly-hybridized character both in commensurate and incommensurate DWNTs with diameter ratios of $\frac{3}{5}$ and with small twists. We propose a nearly-degenerate phonon coupling picture to explain the experiments that is quantitatively supported by our DFT calculations on commensurate DWNTs with fully resolved phonon eigenvectors and eigenvalues. Our work demonstrates the strong phonon-phonon coupling effect in 1D systems for the first time and it can promise the engineering of phonon-phonon coupling and phonon spectra in 1D systems and their moiré superlattices.

Acknowledgements:

This work is mainly supported by Zhejiang Provincial Natural Science Foundation of China (LR23A040002) & National Natural Science Foundation of China (12174335). This work is also supported by National Key R&D Program of China (2023YFA1407900 & 2022YFA1203400). Parts of this study are supported by JSPS KAKENHI (JP24K06968 to TK, 23K23161 to DK). The calculations in this study have been done using the Numerical Materials Simulator at NIMS, and using the facilities of the Supercomputer Center, the Institute for Solid State Physics, the University of Tokyo.

Reference:

- [1] C. Kittel, *Introduction to Solid State Physics* (Wiley, New York, 2005).
- [2] J. Bardeen, L. N. Cooper, and J. R. Schrieffer, Theory of Superconductivity, *Physical Review* **108**, 1175 (1957).
- [3] S. Dai, Z. Fei, Q. Ma, A. S. Rodin, M. Wagner, A. S. McLeod, M. K. Liu, W. Gannett, W. Regan, K. Watanabe *et al.*, Tunable Phonon Polaritons in Atomically Thin van der Waals Crystals of Boron Nitride, *Science* **343**, 1125 (2014).
- [4] R. Peierls, Zur kinetischen Theorie der Wärmeleitung in Kristallen, *Annalen der Physik* **395**, 1055 (1929).

- [5] N. Bonini, M. Lazzeri, N. Marzari, and F. Mauri, Phonon Anharmonicities in Graphite and Graphene, *Physical Review Letters* **99**, 176802 (2007).
- [6] N. K. Ravichandran and D. Broido, Phonon-Phonon Interactions in Strongly Bonded Solids: Selection Rules and Higher-Order Processes, *Physical Review X* **10**, 021063 (2020).
- [7] X. Qian, J. Zhou, and G. Chen, Phonon-engineered extreme thermal conductivity materials, *Nature Materials* **20**, 1188 (2021).
- [8] O. Delaire, J. Ma, K. Marty, A. F. May, M. A. McGuire, M. H. Du, D. J. Singh, A. Podlesnyak, G. Ehlers, M. D. Lumsden *et al.*, Giant anharmonic phonon scattering in PbTe, *Nature Materials* **10**, 614 (2011).
- [9] B. Poudel, Q. Hao, Y. Ma, Y. Lan, A. Minnich, B. Yu, X. Yan, D. Wang, A. Muto, D. Vashaee *et al.*, High-Thermoelectric Performance of Nanostructured Bismuth Antimony Telluride Bulk Alloys, *Science* **320**, 634 (2008).
- [10] O. Hellman and D. A. Broido, Phonon thermal transport in Bi₂Te₃ from first principles, *Physical Review B* **90**, 134309 (2014).
- [11] M.-L. Lin, Q.-H. Tan, J.-B. Wu, X.-S. Chen, J.-H. Wang, Y.-H. Pan, X. Zhang, X. Cong, J. Zhang, W. Ji *et al.*, Moiré Phonons in Twisted Bilayer MoS₂, *ACS Nano* **12**, 8770 (2018).
- [12] M. Koshino and Y.-W. Son, Moiré phonons in twisted bilayer graphene, *Physical Review B* **100**, 075416 (2019).
- [13] J. Quan, L. Linhart, M.-L. Lin, D. Lee, J. Zhu, C.-Y. Wang, W.-T. Hsu, J. Choi, J. Embley, C. Young *et al.*, Phonon renormalization in reconstructed MoS₂ moiré superlattices, *Nature Materials* **20**, 1100 (2021).
- [14] L. P. A. Krishna and M. Koshino, Moiré phonons in graphene/hexagonal boron nitride moiré superlattice, *Physical Review B* **107**, 115301 (2023).
- [15] J. M. Luttinger, An Exactly Soluble Model of a Many-Fermion System, *Journal of Mathematical Physics* **4**, 1154 (1963).
- [16] M. Bockrath, D. H. Cobden, J. Lu, A. G. Rinzler, R. E. Smalley, L. Balents, and P. L. McEuen, Luttinger-liquid behaviour in carbon nanotubes, *Nature* **397**, 598 (1999).
- [17] R. E. Peierls, *Quantum Theory of Solids* (Clarendon Press, Oxford, 1996).
- [18] A. Luther and I. Peschel, Single-particle states, Kohn anomaly, and pairing fluctuations in one dimension, *Physical Review B* **9**, 2911 (1974).
- [19] K. Liu, C. Jin, X. Hong, J. Kim, A. Zettl, E. Wang, and F. Wang, Van der Waals-coupled electronic states in incommensurate double-walled carbon nanotubes, *Nature Physics* **10**, 737 (2014).
- [20] S. Zhao, T. Kitagawa, Y. Miyauchi, K. Matsuda, H. Shinohara, and R. Kitaura, Rayleigh scattering studies on inter-layer interactions in structure-defined individual double-wall carbon nanotubes, *Nano Research* **7**, 1548 (2014).
- [21] G. Gordeev, S. Wasserroth, H. Li, A. Jorio, B. S. Flavel, and S. Reich, Dielectric Screening inside Carbon Nanotubes, *Nano Letters* **24**, 8030 (2024).
- [22] M. Koshino, P. Moon, and Y.-W. Son, Incommensurate double-walled carbon nanotubes as one-dimensional moiré crystals, *Physical Review B* **91**, 035405 (2015).

- [23] S. Zhao, P. Moon, Y. Miyauchi, T. Nishihara, K. Matsuda, M. Koshino, and R. Kitaura, Observation of Drastic Electronic-Structure Change in a One-Dimensional Moiré Superlattice, *Physical Review Letters* **124**, 106101 (2020).
- [24] D. Levshov, T. X. Than, R. Arenal, V. N. Popov, R. Parret, M. Paillet, V. Jourdain, A. A. Zahab, T. Michel, Y. I. Yuzyuk *et al.*, Experimental Evidence of a Mechanical Coupling between Layers in an Individual Double-Walled Carbon Nanotube, *Nano Letters* **11**, 4800 (2011).
- [25] K. Liu, X. Hong, M. Wu, F. Xiao, W. Wang, X. Bai, J. W. Ager, S. Aloni, A. Zettl, E. Wang *et al.*, Quantum-coupled radial-breathing oscillations in double-walled carbon nanotubes, *Nature Communications* **4**, 1375 (2013).
- [26] G. Gordeev, S. Wasserroth, H. Li, B. Flavel, and S. Reich, Moiré-Induced Vibrational Coupling in Double-Walled Carbon Nanotubes, *Nano Letters* **21**, 6732 (2021).
- [27] V. N. Popov and L. Henrard, Breathinglike phonon modes of multiwalled carbon nanotubes, *Physical Review B* **65**, 235415 (2002).
- [28] E. Dobardžić, J. Maultzsch, I. Milošević, C. Thomsen, and M. Damnjanović, The radial breathing mode frequency in double-walled carbon nanotubes: an analytical approximation, *physica status solidi (b)* **237**, R7 (2003).
- [29] A. Rahmani, J. L. Sauvajol, J. Cambedouzou, and C. Benoit, Raman-active modes in finite and infinite double-walled carbon nanotubes, *Physical Review B* **71**, 125402 (2005).
- [30] P. Giannozzi, S. Baroni, N. Bonini, M. Calandra, R. Car, C. Cavazzoni, D. Ceresoli, G. L. Chiarotti, M. Cococcioni, I. Dabo *et al.*, QUANTUM ESPRESSO: a modular and open-source software project for quantum simulations of materials, *Journal of Physics: Condensed Matter* **21**, 395502 (2009).
- [31] P. Giannozzi, O. Andreussi, T. Brumme, O. Bunau, M. Buongiorno Nardelli, M. Calandra, R. Car, C. Cavazzoni, D. Ceresoli, M. Cococcioni *et al.*, Advanced capabilities for materials modelling with Quantum ESPRESSO, *Journal of Physics: Condensed Matter* **29**, 465901 (2017).
- [32] A. Togo, L. Chaput, T. Tadano, and I. Tanaka, Implementation strategies in phonopy and phono3py, *Journal of Physics: Condensed Matter* **35**, 353001 (2023).
- [33] A. Togo, First-principles Phonon Calculations with Phonopy and Phono3py, *Journal of the Physical Society of Japan* **92**, 012001 (2022).
- [34] S. Grimme, J. Antony, S. Ehrlich, and H. Krieg, A consistent and accurate ab initio parametrization of density functional dispersion correction (DFT-D) for the 94 elements H-Pu, *The Journal of Chemical Physics* **132**, 154104 (2010).
- [35] M. Kociak, K. Suenaga, K. Hirahara, Y. Saito, T. Nakahira, and S. Iijima, Linking Chiral Indices and Transport Properties of Double-Walled Carbon Nanotubes, *Physical Review Letters* **89**, 155501 (2002).
- [36] K. Liu, Z. Xu, W. Wang, P. Gao, W. Fu, X. Bai, and E. Wang, Direct determination of atomic structure of large-indexed carbon nanotubes by electron diffraction: application to double-walled nanotubes, *Journal of Physics D: Applied Physics* **42**, 125412 (2009).

- [37]R. Saito, G. Dresselhaus, and M. S. Dresselhaus, Trigonal warping effect of carbon nanotubes, *Physical Review B* **61**, 2981 (2000).
- [38]K. Liu, J. Deslippe, F. Xiao, R. B. Capaz, X. Hong, S. Aloni, A. Zettl, W. Wang, X. Bai, S. G. Louie *et al.*, An atlas of carbon nanotube optical transitions, *Nature Nanotechnology* **7**, 325 (2012).
- [39]K. Liu, W. Wang, M. Wu, F. Xiao, X. Hong, S. Aloni, X. Bai, E. Wang, and F. Wang, Intrinsic radial breathing oscillation in suspended single-walled carbon nanotubes, *Physical Review B* **83**, 113404 (2011).
- [40]S. Piscanec, M. Lazzeri, J. Robertson, A. C. Ferrari, and F. Mauri, Optical phonons in carbon nanotubes: Kohn anomalies, Peierls distortions, and dynamic effects, *Physical Review B* **75**, 035427 (2007).
- [41]R. Saito, G. Dresselhaus, and M. S. Dresselhaus, *Physical Properties of Carbon Nanotubes* (Imperial College Press, London, 1998).
- [42]M. S. Dresselhaus and P. C. Eklund, Phonons in carbon nanotubes, *Advances in Physics* **49**, 705 (2000).

Supplementary Materials

Observation of strong phonon-phonon coupling in one-dimensional van der Waals crystals

Shaoqi Sun¹, Qingyun Lin², Yihuan Li¹, Daichi Kozawa³, Huizhen Wu¹, Shigeo Maruyama⁴, Pilkyung Moon⁵, Toshikaze Kariyado^{3*}, Ryo Kitaura^{3*} and Sihan Zhao^{1*}

1. School of Physics, Interdisciplinary Center for Quantum Information, Zhejiang Key Laboratory of Micro-Nano Quantum Chips and Quantum Control, and State Key Laboratory of Silicon and Advanced Semiconductor Materials, Zhejiang University, Hangzhou 310058, China

2. Center of Electron Microscopy, School of Materials Science and Engineering, Zhejiang University, Hangzhou 310027, China

3. Research Center for Materials Nanoarchitectonics (MANA), National Institute for Materials Science (NIMS), 1-1 Namiki, Tsukuba 305-0044, Japan

4. Department of Mechanical Engineering, The University of Tokyo, Tokyo 113-8656, Japan

5. Arts and Sciences, NYU Shanghai, Shanghai 200124, China; NYU-ECNU Institute of Physics at NYU Shanghai, Shanghai 200062, China

Corresponding authors:

KARIYADO.Toshikaze@nims.go.jp

KITAURA.Ryo@nims.go.jp

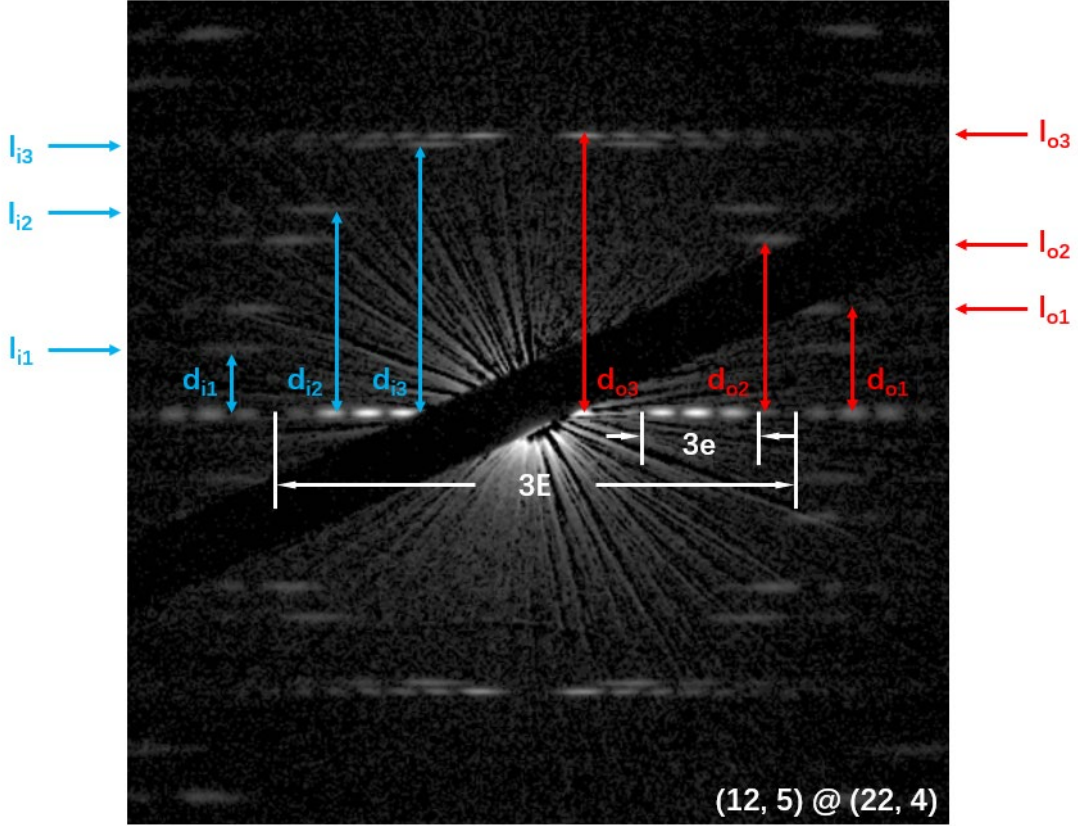
sihanzhao88@zju.edu.cn

Supplementary Note 1.

To investigate the effect of strong phonon coupling in DWNT crystals, we directly grew air-suspended DWNTs with high quality across an open slit ($\sim 30 \mu\text{m}$ in width) by alcohol catalytic chemical vapor deposition (ACCVD). Combined Rayleigh scattering and resonant Raman scattering spectroscopies measured in the same configuration were employed to probe the electronic optical transitions and phonon vibrations for chirality-resolved individual DWNTs. We focused either a supercontinuum laser source (1.2–2.65 eV for Rayleigh) or monochromic laser lines (514, 532, 561 and 633 nm for Raman) on the central part of each suspended DWNT, with the light polarized along each nanotube axis. The light scattered by the nanotube was collected and directed to a CCD camera and a spectrometer. The Rayleigh spectra normalized by the incident light were further corrected by multiplying a factor of $1/E^3$ for different photon energy E to directly reflect the susceptibility of nanotube dipoles. The spectral resolutions for Rayleigh and Raman measurements were about 5 meV and $1\text{--}2 \text{ cm}^{-1}$, respectively. The structure (i.e., the chirality) of each individual DWNT was determined by nanobeam electron diffraction in a transmission electron microscope (TEM) operated at 80 keV (JEM-F200) where diffractions at two ends of the same DWNT were measured to ensure the structural homogeneity and unambiguous assignment over the whole suspended part, further consolidated by simulations. Since electron diffraction cannot distinguish the left-hand species from right-hand ones of chiral SWNTs, we assumed that each DWNT in this study contain two constituent SWNTs with same handedness.

The phonon modes are derived using the density functional theory through Quantum Espresso [1,2] and Phonopy [3,4] packages. First, relaxed lattice structures of single- and double-walled carbon nanotubes have been obtained with the criterion that the maximum force on the atoms went below 0.001 Ry/bohr. In our calculation, we have adapted the projector augmented wave method, taken a pseudopotential from [3,4] and used the PBE-GGA functional [5]. The van der Waals forces were included through DFT-D3 method [6]. The cutoff energies for the wave functions and the charge density were set to 60 Ry and 489 Ry, respectively. The nanotube axis was aligned with z-axis, and for x- and y- directions, the system was assumed to be periodic with the lattice constant 4 nm, which was sufficiently larger than the nanotube diameter. Then, the force constants required for the phonon mode calculation was obtained by perturbing the atomic positions in $1 \times 1 \times 4$ supercell of the above-mentioned relaxed structures for single- and double-walled carbon nanotubes. (The perturbed structures were automatically generated by Phonopy.) The phonon frequencies and mode shapes were given by diagonalizing dynamical matrices consists of the force constants.

Supplementary Note 2.



The electron diffraction pattern of a DWNT contains its structural information, from which the chiral indices $(n_i, m_i) @ (n_o, m_o)$ can be determined unambiguously. Taking $(12, 5) @ (22, 4)$ in the main text (Fig. 1(a)) as an example, the intensity distribution of the equatorial line oscillates with a small period $e \propto 1/\bar{D}$, within an oscillatory envelope of a large period $E \propto 1/\delta D$, where \bar{D} and δD are the average diameter and diameter difference of inner and outer nanotubes, respectively. Moreover, there are two sets of layer lines, $[l_{i1}, l_{i2}, l_{i3}]$ and $[l_{o1}, l_{o2}, l_{o3}]$, in the electron diffraction pattern, originating from inner and outer nanotubes, respectively. The distances between these layer lines and the equatorial line (d_{i1}, d_{i2}, d_{i3}) for inner SWNT and (d_{o1}, d_{o2}, d_{o3}) for outer SWNT, along with the periods of e and E , are decisive experimental inputs obtained from the analysis of electron diffraction to determine the chiral indices $(n_i, m_i) @ (n_o, m_o)$ [7]:

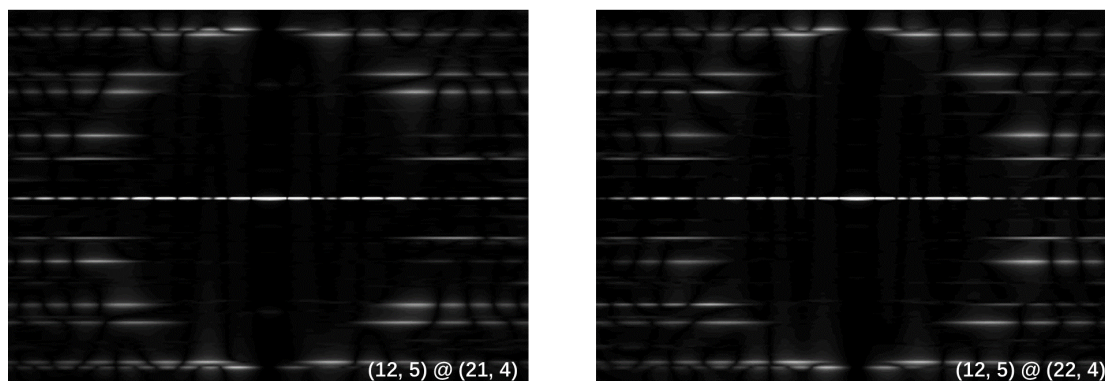
$$\frac{n_o}{\cos \tau} = \frac{\pi}{\sqrt{3}} (2d_{o3} - d_{o2}) \left(\frac{1}{e} + \frac{1}{E} \right) \quad (1)$$

$$\frac{m_o}{\cos \tau} = \frac{\pi}{\sqrt{3}} (2d_{o2} - d_{o3}) \left(\frac{1}{e} + \frac{1}{E} \right) \quad (2)$$

$$\frac{n_i}{\cos \tau} = \frac{\pi}{\sqrt{3}} (2d_{i3} - d_{i2}) \left(\frac{1}{e} - \frac{1}{E} \right) \quad (3)$$

$$\frac{m_i}{\cos \tau} = \frac{\pi}{\sqrt{3}} (2d_{i2} - d_{i3}) \left(\frac{1}{e} - \frac{1}{E} \right) \quad (4)$$

where τ is the tilt angle correction of the nanotube at the substrate edge where the diffraction pattern is taken, and it is usually less than 30° . Using the equations (1)-(4), we can get the chirality candidates of the DWNT being investigated first. After comparing the experimental result with the simulated diffraction patterns of these candidates, we could rule out other possibilities and uniquely determine the chiral indices of the DWNT to be $(12, 5) @ (22, 4)$. The simulated diffraction patterns of two candidates are shown below, in which $(12, 5) @ (22, 4)$ agrees well with the experiment.



Supplementary Note 3.

We observe in Figs. 2(c) and 2(d) in the main text that the RBM frequency blueshift increases with increasing (inner) tube diameter and with decreasing inter-tube distance. The smaller the inter-tube distance, the stronger coupling between two RBMs of inner and outer nanotubes, which explains the latter trend. How to understand the frequency shift becomes larger with decreasing (inner) tube diameter? For large-diameter DWNTs, the RBM frequencies of two pristine inner and outer SWNTs are close to each other, and thus the coupling between inner and outer walls tends to be strong, giving rise to larger frequency blueshifts. This is analogous to a larger energy correction term in second-order perturbation if two unperturbed states are close in energy. By the same token, small-diameter DWNTs show weaker vibrational coupling and smaller frequency blueshifts, so that the vibrational eigenmodes for the in-phase and out-of-phase RBM oscillations are mainly comprised of lattice motions of constituent outer nanotube and inner nanotube, respectively.

Supplementary Table 1.

sample	chirality	inner tube diameter (nm)	outer tube diameter (nm)	diameter difference (nm)	chiral angle difference (°)	resonance	in-phase shift (cm ⁻¹)	out-of-phase shift (cm ⁻¹)	diameter ratio	new peak (cm ⁻¹)
1	(7, 7) @ (12, 12)	0.949	1.628	0.679	0	inner tube	11.87	11.71	0.583	126.7
2	(14, 6) @ (21, 9)	1.392	2.088	0.696	0		17.00	10.21	0.667	
3	(15, 5) @ (23, 7)	1.412	2.129	0.717	1.02		--	7.13	0.663	
4	(9, 5) @ (16, 8)	0.962	1.657	0.695	1.52	outer tube	11.41	--	0.580	
5	(21, 9) @ (27, 13)	2.088	2.767	0.679	1.58		7.50	22.10	0.755	
6	(8, 6) @ (13, 11)	0.953	1.629	0.676	1.96	outer tube	11.96	--	0.585	126.7
7	(10, 7) @ (17, 10)	1.159	1.851	0.692	2.69	inner tube	11.17	9.24	0.626	97.5
8	(14, 5) @ (20, 9)	1.336	2.013	0.677	2.95		8.34	14.34	0.664	
9	(10, 6) @ (15, 11)	1.096	1.770	0.674	3.13	outer tube	12.61	12.89	0.619	116.1
10	(13, 3) @ (22, 3)	1.153	1.851	0.698	3.85	outer tube	16.12	10.65	0.623	
11	(15, 11) @ (23, 13)	1.770	2.472	0.702	4.03		19.67	--	0.716	
12	(13, 5) @ (19, 10)	1.260	1.998	0.738	4.23	outer tube	12.08	--	0.631	
13	(16, 11) @ (25, 12)	1.841	2.560	0.719	5.37	both	--	9.34	0.719	
14	(15, 10) @ (18, 17)	1.707	2.374	0.667	5.64		17.96	24.63	0.719	
15	(12, 5) @ (16, 11)	1.185	1.841	0.656	7.27	inner tube	12.04	18.78	0.644	
16	(17, 16) @ (27, 16)	2.238	2.948	0.710	7.40	outer tube	13.42	18.47	0.759	
17	(12, 5) @ (22, 4)	1.185	1.899	0.714	8.42	outer tube	12.94	7.67	0.624	
18	(12, 4) @ (16, 11)	1.129	1.841	0.712	10.00	outer tube	14.95	--	0.613	
19	(18, 7) @ (29, 3)	1.749	2.397	0.648	10.88	inner tube	11.82	27.11	0.730	
20	(9, 9) @ (19, 9)	1.221	1.939	0.718	11.65	outer tube	15.41	7.07	0.630	
21	(20, 8) @ (32, 3)	1.956	2.631	0.675	11.67	both	14.68	26.96	0.743	
22	(10, 7) @ (21, 6)	1.159	1.923	0.764	11.96	outer tube	7.64	--	0.603	
23	(14, 2) @ (18, 9)	1.182	1.864	0.682	12.52	inner tube	18.38	11.01	0.634	
24	(15, 3) @ (18, 11)	1.308	1.986	0.678	13.12	inner tube	16.31	14.92	0.659	
25	(18, 8) @ (31, 2)	1.806	2.509	0.703	14.38	outer tube	12.59	15.17	0.720	
26	(16, 1) @ (20, 9)	1.294	2.013	0.719	14.65		15.44	7.40	0.643	
27	(13, 11) @ (26, 6)	1.629	2.307	0.678	17.08		18.69	18.82	0.706	
28	(12, 1) @ (15, 10)	0.981	1.707	0.726	19.45	outer tube	6.90	--	0.575	
29	(10, 7) @ (22, 2)	1.159	1.806	0.647	19.87		15.16	24.56	0.642	
30	(18, 4) @ (17, 17)	1.589	2.306	0.717	20.17	both	11.83	10.25	0.689	
31	(21, 17) @ (41, 3)	2.582	3.334	0.752	23.02	inner tube	--	11.12	0.774	

Table S1. Statistics for 31 individual DWNTs in this study. Four DWNTs showing new phonon modes are marked in red. The excitation energy of Raman measurement can be resonant with inner tube or outer tube or both. The “resonance” condition for three DWNTs are left blank because the optical transitions from inner and outer

nanotubes are too close to be distinguishable in Rayleigh spectra. It is noticeable that 10 out of 31 DWNTs ($N = 3, 4, 6, 11, 12, 13, 18, 22, 28, 31$) show only one RBM oscillation which is presumably caused by the off-resonance condition, as the excitation is only resonant with either inner or outer tube. For sample $N = 13$, although the excitation energy is resonant with both nanotubes, the in-phase oscillation is absent.

Supplementary Figure 1.

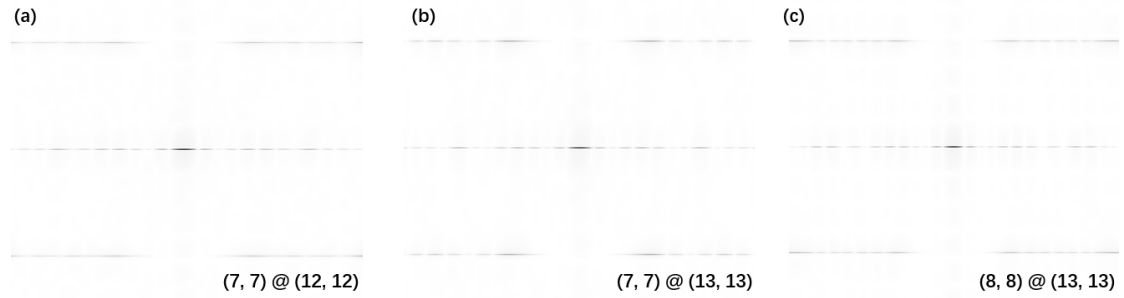


Fig. S1. Simulated diffraction patterns of candidate DWNTs by using an analytical approach [8]. (a) $(7, 7) @ (12, 12)$, (b) $(7, 7) @ (13, 13)$, (c) $(8, 8) @ (13, 13)$. It is apparent that only (a) matches the experimental result shown in Fig. 3(a) in the main text.

Supplementary Figure 2.

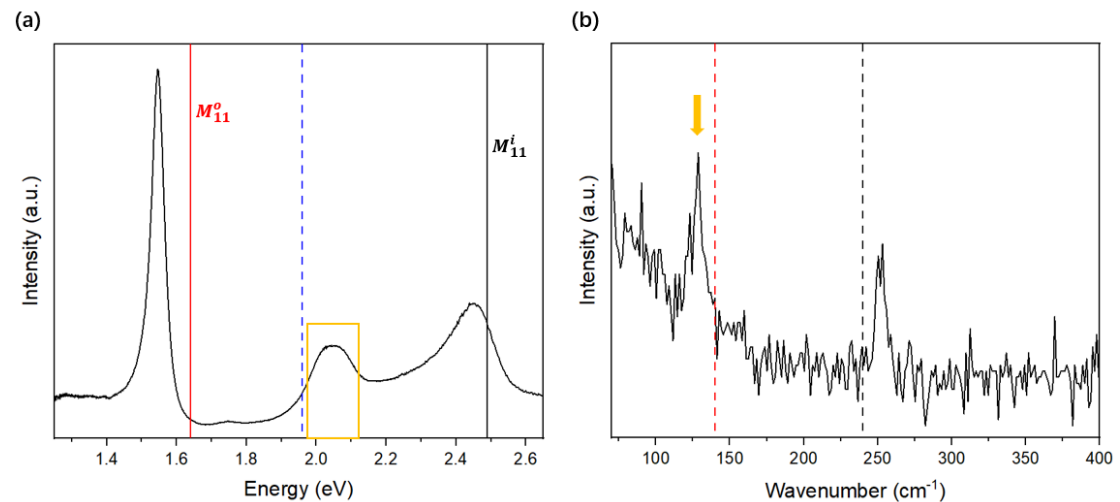


Fig. S2. The Raman spectrum (b) of $(7, 7) @ (12, 12)$ in the low frequency region with the excitation energy of ~ 1.96 eV indicated by the blue dashed line in its Rayleigh spectrum (a). The excitation energy is close to the emerging optical transitions that cannot be attributed to electronic transitions of neither inner nor outer nanotubes. The new phonon mode, indicated by gold arrow in Fig. S2(b), is still present without frequency shift, though the in-phase RBM oscillation is absent, primarily owing to the

weak intensity. The RBM oscillations for pristine inner and outer nanotubes are indicated by the black and red dashed lines.

Supplementary Figure 3.

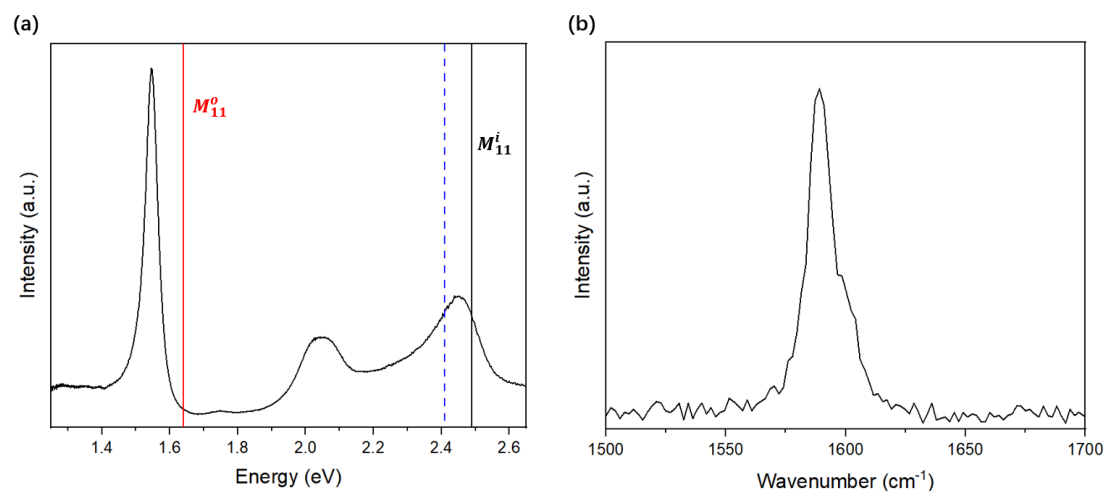


Fig. S3. The resonant Raman spectrum (b) of (7, 7) @ (12, 12) in the G-band region with the excitation energy of ~ 2.41 eV (same as in Fig. 3(c) in the main text), indicated by the blue dashed line in its Rayleigh spectrum (a). The line shape of G mode is asymmetric, and contains multiple peaks.

Supplementary Note 4.

The “strong-coupling” condition for electronic inter-tube interactions in DWNTs is that the chiral vectors of inner and outer nanotubes, C_{in} and C_{out} , are nearly parallel to each other and, at the same time, the difference of the two vectors, $C_{out} - C_{in}$, is strictly along the armchair direction [9]. As a certain DWNT matches the “strong-coupling” criterion, the electronic states of the components strongly hybridize with each other due to the presence of moiré superlattice potential, leading to strong electronic band reconstruction. For (8, 6) @ (13, 11) and (10, 6) @ (15, 11), the differences in chiral angle of the inner and outer nanotubes are $\sim 1.96^\circ$ and $\sim 3.13^\circ$, respectively, and the chiral vector differences, $C_{out} - C_{in}$, are both (5,5), parallel to the armchair direction. Therefore, (8, 6) @ (13, 11) and (10, 6) @ (15, 11) are both strongly-coupled incommensurate DWNTs, whose electronic band structures can be significantly modified by the moiré potential. Indeed, their Rayleigh spectra (Figs. 3(e) and 3(h) in the main text) exhibit pronounced deviation from the perturbation theory, manifesting as pronounced energy shift outside the range between -200 meV and +50 meV and/or the emergence of new optical transitions. The commensurate DWNT (7,7) @ (12,12) also satisfies the “strong-coupling” condition.

Supplementary Figure 4.

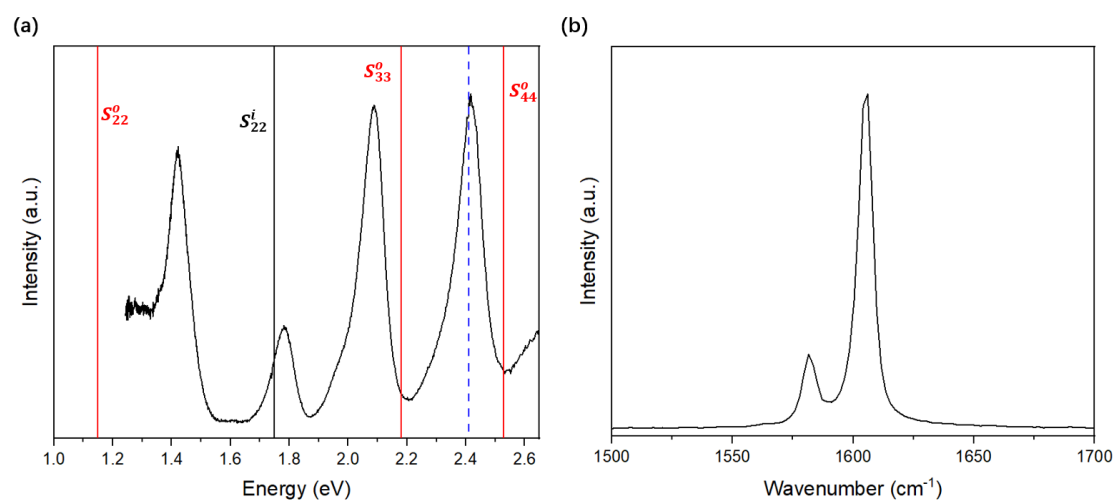


Fig. S4. The resonant Raman spectrum (b) of (8, 6) @ (13, 11) in the G-band region. A clear splitting of G-band is observed. The excitation energy is the same as in Fig. 3(f) in the main text and is indicated by the blue dashed line in its Rayleigh spectrum (a).

Supplementary Figure 5.

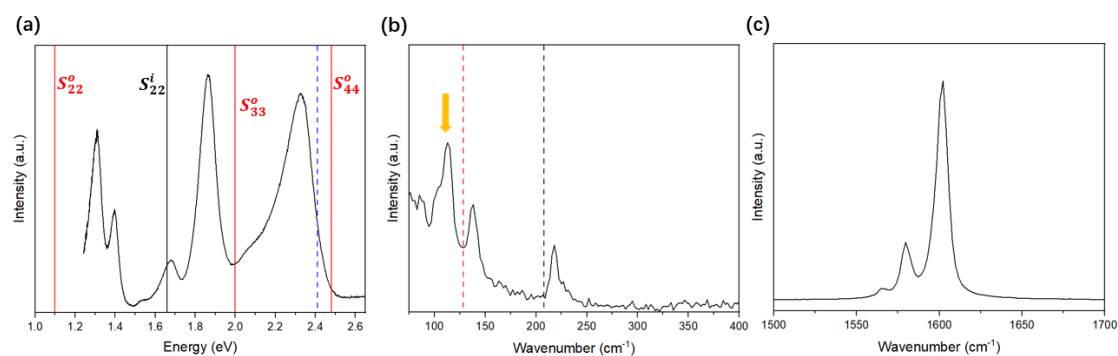


Fig. S5. Raman measurement of DWNT (10, 6) @ (15, 11) with a different excitation energy. The Raman spectra of (10, 6) @ (15, 11) in the low frequency (b) and G-band region (c). The excitation energy at ~ 514 nm is different from Fig. 3(i) in the main text and is indicated by the blue dashed line in the Rayleigh spectrum (a). The Raman spectrum in Fig. S5(b) is similar to Fig. 3(i) in the main text.

Supplementary Figure 6.

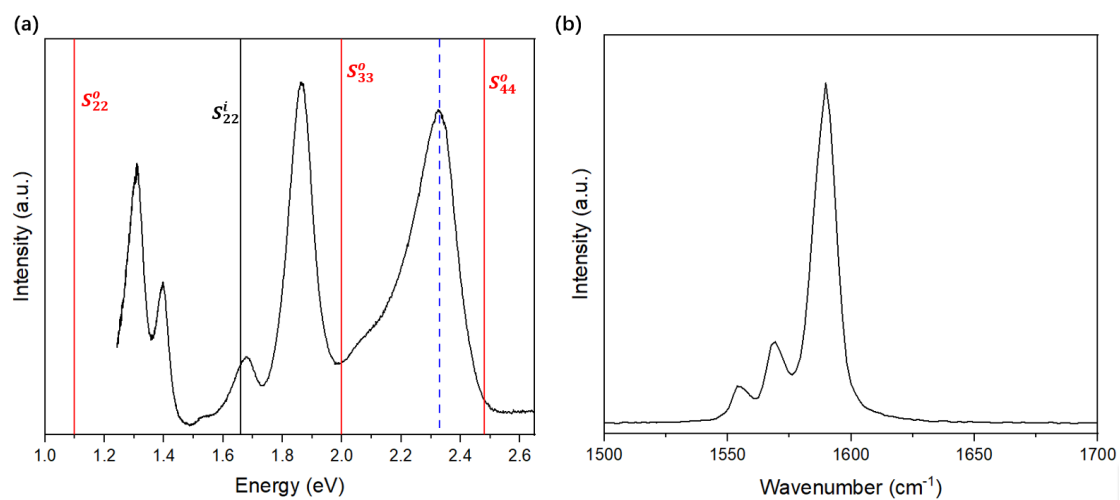
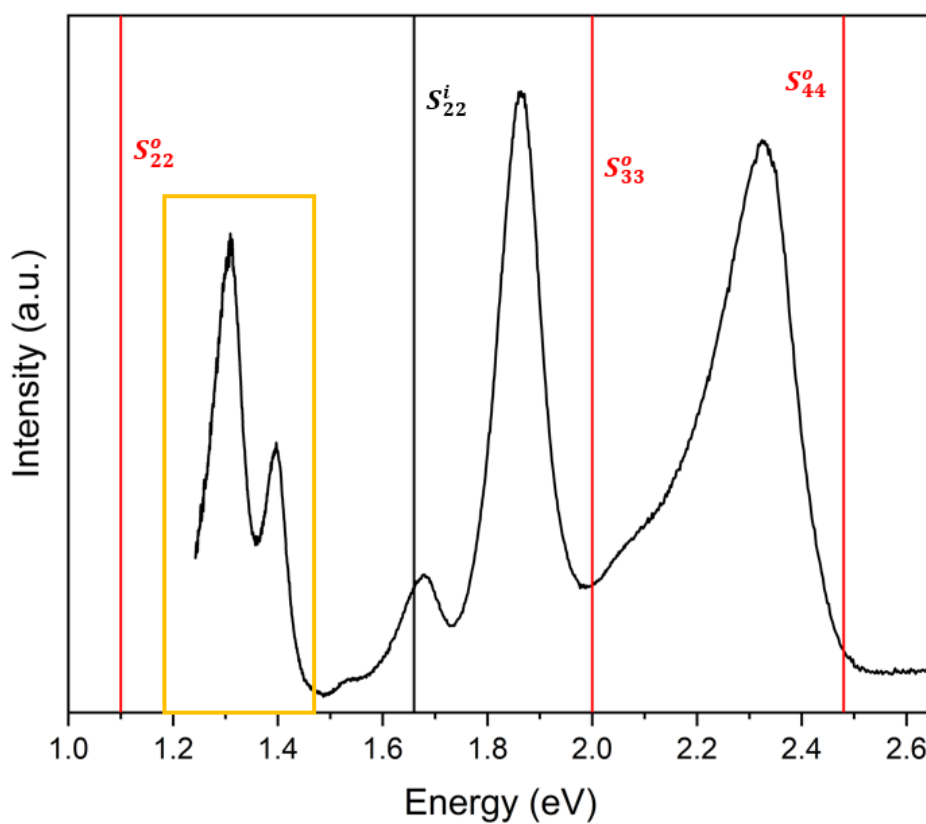


Fig. S6. The Raman spectrum (b) of (10, 6) @ (15, 11) in the G-band region. A clear splitting of G-band into multiple peaks is observed. The excitation energy at ~ 532 nm is the same as in Fig. 3(i) in the main text and is indicated by the blue dashed line in its Rayleigh spectrum (a).

Supplementary Note 5.



The Rayleigh spectrum of (10, 6) @ (15, 11) shows five distinct optical resonances at about 1.31, 1.40, 1.68, 1.86 and 2.33 eV in the range of 1.25-2.65 eV. The optical transitions of pristine (10,6) and (15,11) are indicated by the black and red lines, respectively. The three high-energy peaks at 1.68, 1.86 and 2.33eV can be assigned to S_{22}^i transition of inner tube (10, 6), S_{33}^o and S_{44}^o transitions of outer tube (15,11), respectively, with moderate energy shifts of about 20, -140 and -150 meV. But for the two peaks at lower energy side (framed in gold), they cannot be explained in the framework of perturbation theory. Even though the resonance at ~ 1.31 eV can be assigned to the S_{22}^o transition of outer tube (a blueshift of about +210 meV is already beyond the perturbation theory [10]), the resonance peak at ~ 1.40 eV cannot be assigned to neither pristine inner nor outer nanotube. The Rayleigh spectrum suggests that the electronic band structure of (10, 6) @ (15, 11) reconstructs dramatically as predicted for DWNTs in the “strong-coupling” regime [9].

Supplementary Figure 7.

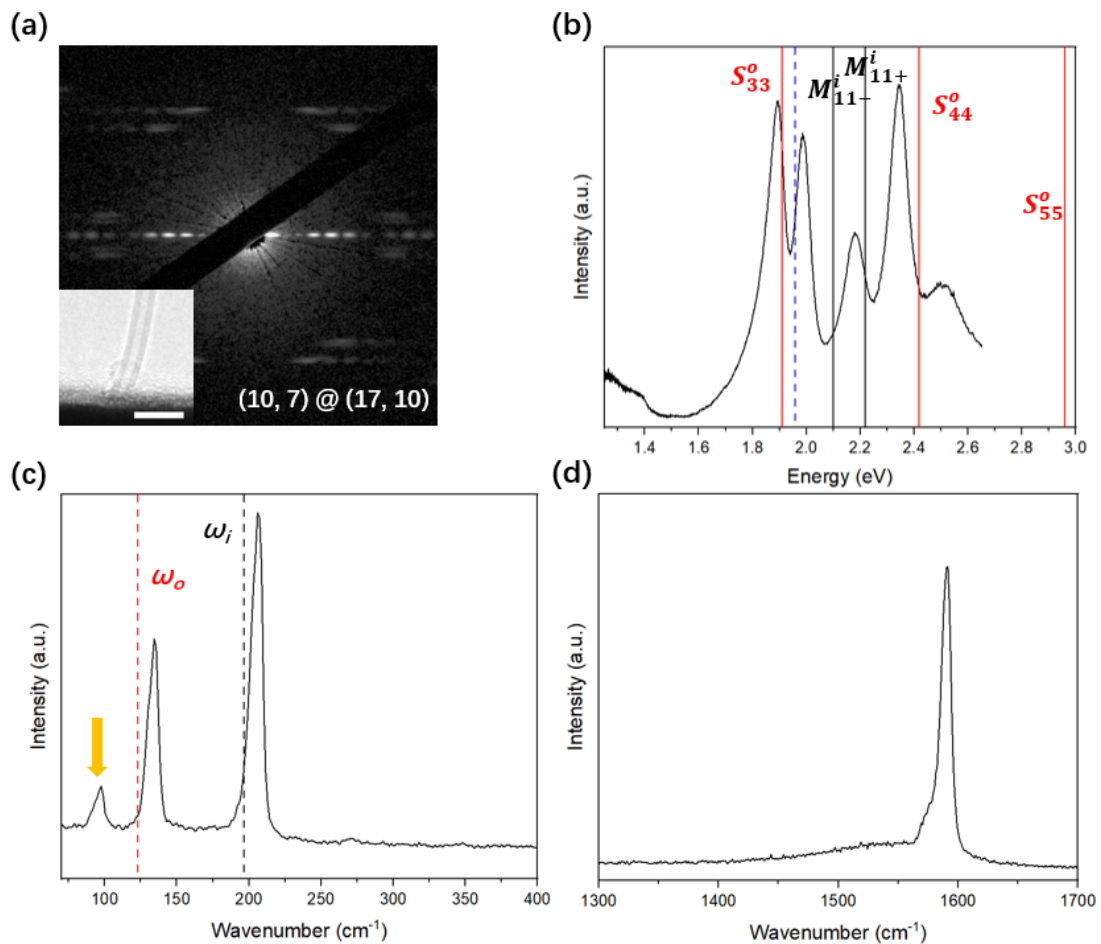


Fig. S7. Characterization of an incommensurate DWNT (10, 7) @ (17, 10), in which strong phonon-phonon coupling occurs. (a) Electron diffraction pattern and TEM image (inset) of (10, 7) @ (17, 10). Scale bar, 5nm. (b) Rayleigh spectrum of (10, 7) @ (17, 10). The optical transitions of pristine inner and outer nanotubes are indicated

by the black and red solid lines, respectively. Excitation energy of ~ 1.96 eV for Raman measurement is indicated by the blue dashed line. (c, d) Raman spectra of the same DWNT in the low frequency (c) and G-band region (d). The black and red dashed lines in (c) indicate the RBM frequencies of pristine inner and outer nanotubes, respectively. An emerging phonon mode, indicated by the gold arrow, is observed at lower frequency with respect to those of the in-phase and out-of-phase oscillations.

Supplementary Figure 8.

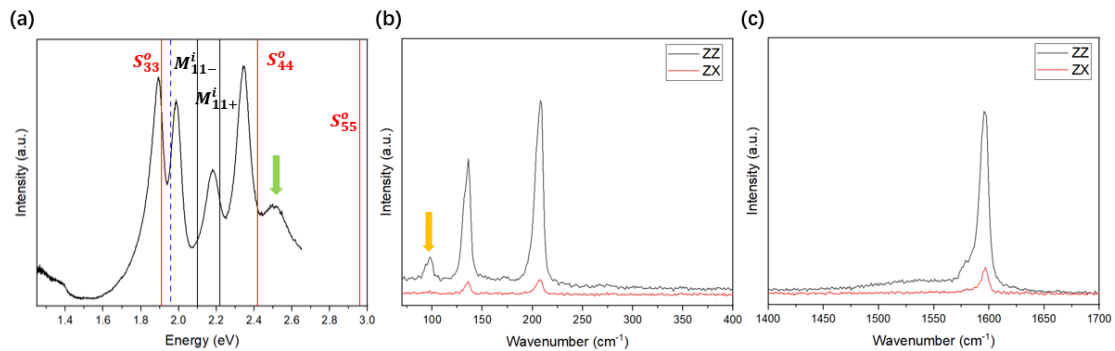


Fig. S8. Polarization-dependent Raman measurement on DWNT (10, 7) @ (17, 10). The Raman spectra of (10, 7) @ (17, 10) in the low frequency (b) and G-band region (c) with different polarization configurations. The excitation energy of ~ 1.96 eV is indicated by the blue dashed line in the corresponding Rayleigh spectrum (a). The new phonon mode in (b) shows a favorable polarization in the ZZ configuration and vanishes in the ZX configuration, where ZZ means the incident and outgoing fields are polarized along tube axis and that ZX means that the incident and outgoing fields are polarized along the tube and circumferential direction. The result means that the new phonon mode is not E_{1g} symmetrywise, but likely to be A_{1g} symmetrywise as for the pristine RBMs. The residue ZX signals for the in-phase and out-of-phase oscillations (b) and G mode (c) are due to the imperfect nanotube placement with respect to the two orthogonal polarizers.

Supplementary Figure 9.

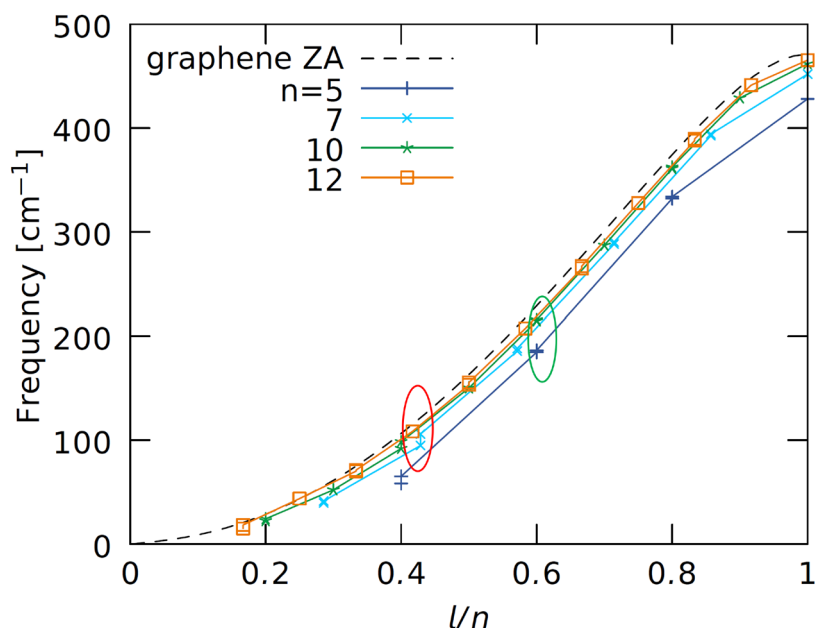


Fig. S9. Calculated eigenvalues for out-of-plane transverse acoustic modes (ZA modes) as a function of l/n for armchair nanotubes (n,n) with $n=5, 7, 10$ and 12 . The two nearly degenerate ZA modes ($l=3$ for $(7,7)$ and $l=5$ for $(12,12)$) that are responsible for the new phonon mode in $(7,7)$ @ $(12,12)$ are highlighted by the red circle. The curvature effect is noticeable as the ZA mode eigenvalues deviate more and more from those of 2D graphene as n is reduced. This suggests that curvature effect needs to be taken into account in addition to the quantum confinement (i.e., zone folding scheme) to evaluate the coupling condition for small-diameter nanotubes. The green circle highlights the curvature effect on ZA mode eigenvalues for $(5,5)$ and $(10,10)$, which makes the otherwise degenerate two states ($l=3$ for $(5,5)$ and $l=6$ for $(10,10)$) have different energies.

Supplementary Figure 10.

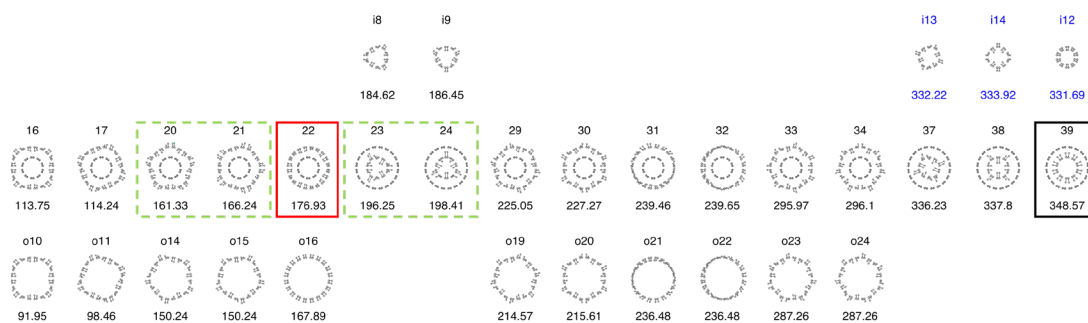


Fig. S10. DFT calculations on the phonon eigenmodes and eigenvalues for DWNT $(5,5)$ @ $(10,10)$ with a diameter ratio of $\frac{1}{2}$. The selected phonon eigenvectors and

eigenvalues in the range between 95 cm^{-1} and 350 cm^{-1} obtained by the calculation are shown. (The omitted modes have no radial components in their eigenvectors, indicating negligible inter-tube couplings.) The coupled vibrational eigenvectors are shown in the middle row, while those for pristine inner and outer nanotubes are shown in the top and bottom rows. The red and black solid frames mark the weakly-coupled in-phase and out-of-phase RBM modes. Green dashed lines mark the coupled modes as a result of mixing of four ZA modes among i8, i9, o14 and o15. This coupling is not strong as the motions of the four modes 20, 21, 23 and 24 are dominated by motion of either inner or outer wall. The large energy mismatch between i7/i8 and o14/o15 leads to the weak phonon coupling, in contrast to the (7,7) @ (12,12) in the main text. We note that the curvature effect is also important to observe strong phonon-phonon coupling. For example, considering quantum confinement (i.e., zone folding) only would predict a strong coupling between i8/i9 (ZA mode with $l=3$) and o19/o20 (ZA mode with $l=6$) for the diameter ratio between inner (5,5) and outer (10,10) is $\frac{1}{2}$. However, the DFT results including the curvature effect show that they have very different energies (see Fig. S9).

Supplementary Note 6.

Suppose a one-dimensional system consists of two periods l_1 and l_2 with $l_1 < l_2$. Then, there arises a moiré period L , which contains $s + 1$ units of l_1 cell and s units of l_2 cell. Then, we have $L = (s + 1)l_1 = sl_2$. From this, $s = l_1/(l_2 - l_1)$ and $L = l_1l_2/(l_2 - l_1)$ are derived. When s is an integer, the moiré period matches to the period of the underlying lattice. When s is a non-integer rational number, the underlying lattice is periodic, but its period does not match to the moiré period. If s is an irrational number, the underlying lattice is aperiodic.

In nanotubes, it is convenient to use azimuthal angle as a coordinate. A (n, n) -nanotube (i.e., armchair nanotube) has a period of $2\pi/n$ in the azimuthal angle space. For double-walled armchair nanotubes, we have $l_1 = 2\pi/n_{\text{outer}}$ and $l_2 = 2\pi/n_{\text{inner}}$, which leads to $L = 2\pi/(n_{\text{outer}} - n_{\text{inner}})$. On the other hand, for the armchair cases, $n_{\text{outer}} - n_{\text{inner}} = 5$ is the condition for realistic fabrication of a double-walled carbon nanotube, since it makes its inter-tube distance well matches to the layer distance in bilayer graphene. Then, local environments along the azimuthal direction change with the period of $2\pi/5$, which accounts the pentagonal distortions assuming that the inter-tube phononic coupling is fixed by local environments.

References:

- Ceresoli, G. L. Chiarotti, M. Cococcioni, I. Dabo *et al.*, QUANTUM ESPRESSO: a modular and open-source software project for quantum simulations of materials, *Journal of Physics: Condensed Matter* **21**, 395502 (2009).
- [2] P. Giannozzi, O. Andreussi, T. Brumme, O. Bunau, M. Buongiorno Nardelli, M. Calandra, R. Car, C. Cavazzoni, D. Ceresoli, M. Cococcioni *et al.*, Advanced capabilities for materials modelling with Quantum ESPRESSO, *Journal of Physics: Condensed Matter* **29**, 465901 (2017).
- [3] A. Togo, L. Chaput, T. Tadano, and I. Tanaka, Implementation strategies in phonopy and phono3py, *Journal of Physics: Condensed Matter* **35**, 353001 (2023).
- [4] A. Togo, First-principles Phonon Calculations with Phonopy and Phono3py, *Journal of the Physical Society of Japan* **92**, 012001 (2022).
- [5] A. Dal Corso, Pseudopotentials periodic table: From H to Pu, *Computational Materials Science* **95**, 337 (2014).
- [6] S. Grimme, J. Antony, S. Ehrlich, and H. Krieg, A consistent and accurate ab initio parametrization of density functional dispersion correction (DFT-D) for the 94 elements H-Pu, *The Journal of Chemical Physics* **132**, 154104 (2010).
- [7] K. Liu, Z. Xu, W. Wang, P. Gao, W. Fu, X. Bai, and E. Wang, Direct determination of atomic structure of large-indexed carbon nanotubes by electron diffraction: application to double-walled nanotubes, *Journal of Physics D: Applied Physics* **42**, 125412 (2009).
- [8] M. Gao, J. M. Zuo, R. Zhang, and L. A. Nagahara, Structure determinations of double-wall carbon nanotubes grown by catalytic chemical vapor deposition, *Journal of Materials Science* **41**, 4382 (2006).
- [9] M. Koshino, P. Moon, and Y.-W. Son, Incommensurate double-walled carbon nanotubes as one-dimensional moiré crystals, *Physical Review B* **91**, 035405 (2015).
- [10] K. Liu, C. Jin, X. Hong, J. Kim, A. Zettl, E. Wang, and F. Wang, Van der Waals-coupled electronic states in incommensurate double-walled carbon nanotubes, *Nature Physics* **10**, 737 (2014).